

Carbon-Iron Electron Transport Channels in Porphyrin–Graphene Complex for ppb-Level Room Temperature NO Gas Sensing

Gao, Yixun; Wang, Jianqiang; Feng, Yancong; Cao, Nengjie; Li, Hao; de Rooij, Nicolaas Frans; Umar, Ahmad; French, Paddy J.; Wang, Yao; Zhou, Guofu

DOI

[10.1002/sml.202103259](https://doi.org/10.1002/sml.202103259)

Publication date

2022

Document Version

Final published version

Published in

Small

Citation (APA)

Gao, Y., Wang, J., Feng, Y., Cao, N., Li, H., de Rooij, N. F., Umar, A., French, P. J., Wang, Y., & Zhou, G. (2022). Carbon-Iron Electron Transport Channels in Porphyrin–Graphene Complex for ppb-Level Room Temperature NO Gas Sensing. *Small*, 18(11), Article 2103259. <https://doi.org/10.1002/sml.202103259>

Important note

To cite this publication, please use the final published version (if applicable). Please check the document version above.

Copyright

Other than for strictly personal use, it is not permitted to download, forward or distribute the text or part of it, without the consent of the author(s) and/or copyright holder(s), unless the work is under an open content license such as Creative Commons.

Takedown policy

Please contact us and provide details if you believe this document breaches copyrights. We will remove access to the work immediately and investigate your claim.

Green Open Access added to TU Delft Institutional Repository

'You share, we take care!' - Taverne project

<https://www.openaccess.nl/en/you-share-we-take-care>

Otherwise as indicated in the copyright section: the publisher is the copyright holder of this work and the author uses the Dutch legislation to make this work public.

Carbon–Iron Electron Transport Channels in Porphyrin–Graphene Complex for ppb-Level Room Temperature NO Gas Sensing


Yixun Gao, Jianqiang Wang, Yancong Feng, Nengjie Cao, Hao Li, Nicolaas Frans de Rooij, Ahmad Umar, Paddy J. French, Yao Wang,* and Guofu Zhou

It is a great challenge to develop efficient room-temperature sensing materials and sensors for nitric oxide (NO) gas, which is a biomarker molecule used in the monitoring of inflammatory respiratory diseases. Herein, Hemin (Fe (III)-protoporphyrin IX) is introduced into the nitrogen-doped reduced graphene oxide (N-rGO) to obtain a novel sensing material HNG-ethanol. Detailed XPS spectra and DFT calculations confirm the formation of carbon–iron bonds in HNG-ethanol during synthesis process, which act as electron transport channels from graphene to Hemin. Owing to this unique chemical structure, HNG-ethanol exhibits superior gas sensing properties toward NO gas ($R_a/R_g = 3.05$, 20 ppm) with a practical limit of detection (LOD) of 500 ppb and reliable repeatability (over 5 cycles). The HNG-ethanol sensor also possesses high selectivity against other exhaled gases, high humidity resistance, and stability (less than 3% decrease over 30 days). In addition, a deep understanding of the gas sensing mechanisms is proposed for the first time in this work, which is instructive to the community for fabricating sensing materials based on graphene-iron derivatives in the future.

Y. Gao, J. Wang, Y. Feng, N. Cao, H. Li, N. F. de Rooij, Y. Wang, G. Zhou
National Center for International Research on Green Optoelectronics
Guangdong Provincial Key Laboratory of Optical Information Materials
and Technology
Institute of Electronic Paper Displays
South China Academy of Advanced Optoelectronics
South China Normal University
Guangzhou 510006, P. R. China
E-mail: wangyao@m.scnu.edu.cn

A. Umar
Promising Centre for Sensors and Electronic Devices
Department of Chemistry
Faculty of Science and Arts
Najran University
Najran 11001, Kingdom of Saudi Arabia

P. J. French
BE Laboratory
EWI
Delft University of Technology
Delft 2628CD, The Netherlands

 The ORCID identification number(s) for the author(s) of this article can be found under <https://doi.org/10.1002/smll.202103259>.

DOI: 10.1002/smll.202103259

1. Introduction

Nitric oxide (NO), an active small molecule, plays a vital and diverse role in the regulation of physiological processes.^[1] Considerable evidences successively show that the measurement of Fractional exhaled nitric oxide (FeNO) is an effective non-traumatic method for assessment of inflammatory respiratory diseases, as a beneficial complement to clinical diagnosis.^[2] Nevertheless, because of the high reactivity but specific oxidability of NO (lower than NO₂ but higher than other non-oxidizing gas), it remains challenging in the improvement of NO gas sensors to meet the ever-increasing demand for clinical applications.

Traditional detection methods for NO gas often depend on bulky instruments with high expense, which could hardly satisfy the requirement of facile diagnosis and treatment.^[3] Metal oxide semiconductor (MOS), such as ZnO,^[4] WO₃,^[5]

SnO_x,^[6] etc., are widely focused on for NO gas sensing via chemoresistive methods in recent years. However, due to their low conductivity and poor surface activity under ambient conditions, these gas sensors typically work at elevated temperature (often >180 °C), which would cause high energy consumption and fire hazards. Based on fluorescent sensing, organic molecules and polymers with structures such as phenylamine and o-phenylenediamine exhibited excellent performances for NO gas sensing at room temperature,^[7] but complicated synthesis process and poor response reversibility derived from their chemical reactive mechanisms limited their practical applications.

In recent years, kinds of novel metallic materials have been developed by several research groups to realize room temperature NO gas sensing with high reversibility and selectivity.^[8] Generally hybridized with carbon-based materials and fabricated into unique nanostructures, these metallic materials could effectively interact with NO molecule via the metal atoms as active sites. Nevertheless, insufficient sensing properties and the requirement of energy input such as UV-light have hindered their practical applications in clinical assessment and diagnosis. The development of novel high-performance

materials and the establishment of recognized sensing mechanisms are of significance for the practical application if NO gas sensors.

Considering their chelate structures, researches on metal porphyrin derivatives (porphyrin, phthalocyanine, corrole, etc.) are widespread, especially in areas of molecular probes and sensors.^[9] It was demonstrated that the heterocyclic structure of porphyrin could perform excellent gas absorption,^[10] while chelated metal ions such as Fe²⁺ and Co²⁺ could act as selective catalyst for oxidation/reduction, resulting in efficient specific recognition of NO.^[11] However, isolated porphyrin molecule with poor electroconductivity is difficult to show chemoresistive response. Recently, graphene and its derivatives are considered to be very promising materials for room temperature gas sensing.^[12] The doping of heteroatoms such as nitrogen or boron, is gradually served as a regular method to effectively modify the electrical properties of graphene for applications.^[13] Moreover, theoretical studies on single-atom catalysis have demonstrated that it is feasible and beneficial for charge transfer to construct carbon–iron (C–Fe) bonds in graphene-metal derivatives.^[14] Inspired by these previous works, it is reasonable to propose that the combination between porphyrin and the electron-conductive N-doped graphene could construct C–Fe bonds as effective charge transfer channels, which would “empower” porphyrin with the capability to express the chemoresistive response toward NO gas.

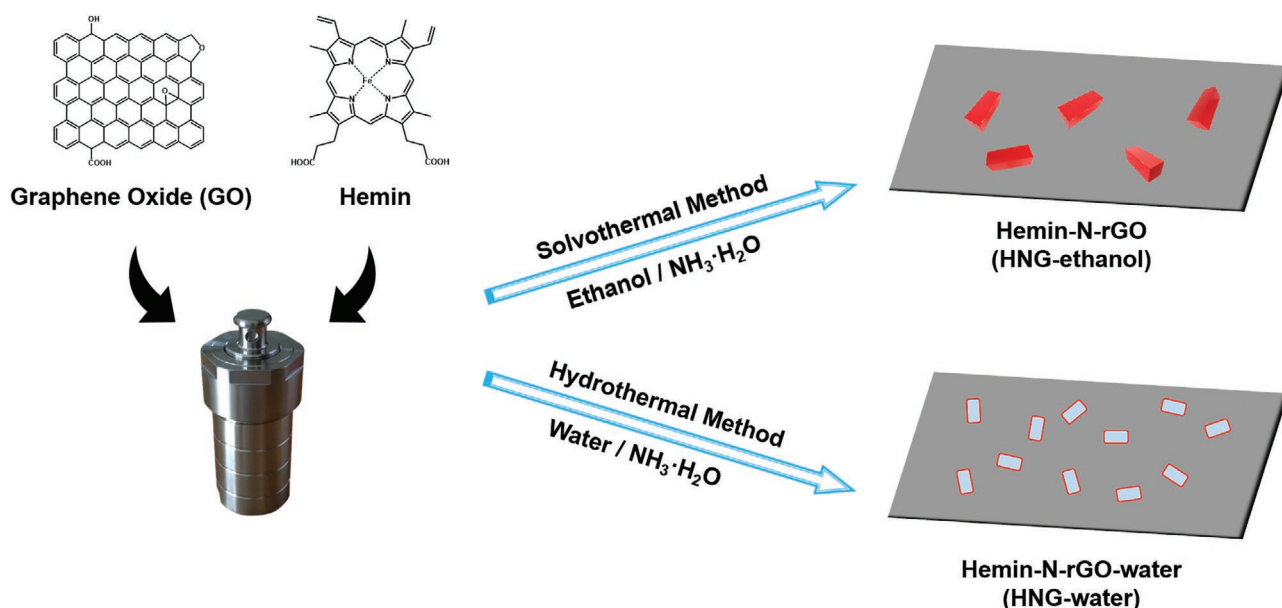
In this work, Hemin, namely Fe (III)-protoporphyrin IX, was employed for the combination with nitrogen-doped reduced graphene oxide (N-rGO) to fabricate an NO gas sensing material Hemin-N-doped-graphene (HNG-ethanol). The sensor exhibited outstanding sensing performances ($R_a/R_g > 300\%$, response time ≤ 500 s). Meanwhile, the sensing mechanism of the HNG-ethanol sensor was further explored via both experimental methods and density functional theory (DFT) calculations. It was proposed for the first time that the C–Fe bonds on the surface of graphene could act as the electron transport

channel from graphene to NO molecule, which determined the sensing properties of HNG-ethanol. This work provides a fresh strategy of fabricating carbon-based metallic materials for room temperature NO sensing.

2. Results and Discussion

The synthesis process was illustrated in **Scheme 1**. Graphene oxide (GO) and Hemin were composed via a simple solvothermal method in ethanol, yielding suspension liquid of Hemin-N-rGO (HNG-ethanol). A similar hydrothermal process with the only substitution of water for ethanol was carried out to obtain suspension liquid of Hemin-N-rGO-water (HNG-water). In addition, control group without the introduction of Hemin was carried out to obtain N-rGO for comparison.

The Raman spectra for GO and N-rGO presented the main features of graphene-based materials (Figure S1, Supporting Information). After reduction and combination, three characteristic sharp peaks of Hemin at 1360 cm⁻¹, 1560 cm⁻¹ and 1610 cm⁻¹ remained in the Raman spectra of HNG-ethanol and HNG-water, confirming the successful attachment of Hemin to the graphene after three-time rinsing, respectively. The functional groups of N-rGO, Hemin, HNG-ethanol, and HNG-water were characterized by Fourier transform infrared spectroscopy (FT-IR), respectively. As shown in Figure S2, Supporting Information, the vibration peaks of N–H stretching and C–N from pyridine in N-rGO confirmed the successful reduction of GO. After the combination between N-rGO and Hemin, typical peaks of both appeared in the FT-IR spectra of HNG-ethanol. However, no characteristic peak of Hemin was found for HNG-water. The sharp peak at 1710 cm⁻¹ in Hemin red-shifted to 1580 cm⁻¹ in HNG-water, which could be ascribed to the formation of the carboxylate. Besides, the broad peak at 3410 cm⁻¹ in HNG-water should be attributed to the strong hydrogen bonding happened between Hemin and rGO in HNG-water.



Scheme 1. Synthesis process of HNG-ethanol and HNG-water.

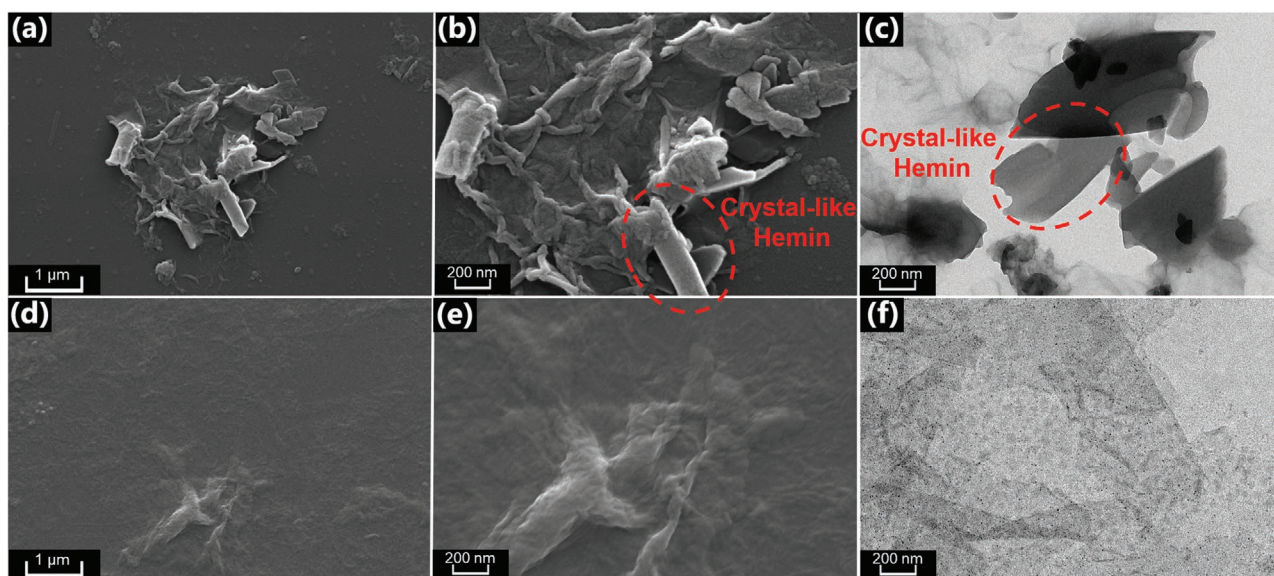


Figure 1. SEM images of a,b) HNG-ethanol and d,e) HNG-water. TEM images of c) HNG-ethanol and f) HNG-water. The crystal-like Hemin was marked by red circles.

The morphology and nanostructure of the as-prepared products were examined through TEM and SEM. As shown in **Figure 1a–c**, large aggregates with crystal-like morphology were observed for HNG-ethanol samples, while only gauzy graphene nanosheets were found in the TEM and SEM images of HNG-water (**Figure 1d–f**). To identify the contents of the aggregates, powder X-ray diffraction (XRD) patterns of HNG-ethanol, HNG-water, Hemin and GO were obtained (**Figure S3**, Supporting Information), respectively. The characteristic peak of GO was absent in both patterns of HNG-ethanol and HNG-water, because the successful introduction of Hemin destroyed the layered structure of graphene sheets. Sharp diffraction peaks with similar distribution were found in both patterns of HNG-ethanol and Hemin, which are consistent with that of the previously reported Hemin aggregates.^[15] However, no such peaks existed in the pattern of HNG-water, indicating that the aggregates in HNG-ethanol were probably the crystalline Hemin. The SEM image of the control group without adding graphene oxide showed that clusters of Hemin crystalline rods were also generated with the absence of graphene (**Figure S4**, Supporting Information).

To investigate the sensing properties of Hemin aggregates on graphene, the as-prepared rGO, HNG-ethanol, and HNG-water were employed as sensing materials to fabricate the sensors on Ag–Pd interdigitated electrodes (IEs), respectively. Gas sensing tests were carried out for NO gas (N₂ as background gas) at an operating temperature of 25 °C.

As shown in **Figure 2a**, the HNG-ethanol sensor exhibited a significantly enhanced response ($R_a/R_g = 3.05$) toward 20 ppm of NO gas, compared to N-rGO and HNG-water. After purging the chamber with air, the response of HNG-ethanol recovered to 100% of the initial value in despite of a relatively long recovery time (1500 s). It should be noted that the low response of HNG-water toward NO was not due to the absence of Hemin, since the XPS spectra of HNG-water (**Figure 3**) verified the existence of Fe. Moreover, an excellent linear relationship

(**Figure 2b**) between gas concentration (0.5–20 ppm) and sensitivity, and good sensing repeatability (**Figure 2c**) toward NO at room temperature were illustrated in **Figure 2**. The gradually increased recovery time could be caused by the slower diffusion of NO after more response-recovery cycles. For comparison, all the reported room temperature NO gas sensors based on metal derivatives (metal oxide, metal nanoparticles, metal complex, etc.) and our work were summarized in **Table 1**. To the best of our knowledge, HNG-ethanol should be regarded as top of the most promising NO gas sensing metallic materials so far.

Generally, the selectivity and stability of sensors were highly required for practical application in medical research and clinical diagnosis. As shown in **Figure 2d**, the HNG-ethanol sensor exhibited a much higher response toward NO ($R_a/R_g = 3.05$, 20 ppm) than other exhaled gases including ammonia ($R_a/R_g = 1.14$, 20 ppm), acetone ($R_a/R_g = 1.03$, 20 ppm), ethanol ($R_a/R_g = 1.04$, 20 ppm), and water ($R_a/R_g = 1.02$, 200 ppm). Its good selectivity to NO could be ascribed to the specific interaction between Hemin and NO molecules. To investigate the stability of our sensing material, an aging test of the HNG-ethanol sensor was carried out for over a month (**Figure 2e**). The response of HNG-ethanol remained about 98% of the initial value after 30 days, indicating its excellent stability. As another important interferent, water would inevitably exist in the exhaled gas. As shown in **Figure 2f**, the responses of HNG-ethanol under 0–75% relative humidity were 3.05, 3.38, 3.26, and 3.06, respectively, with a standard deviation of 4.6%. To the best of our knowledge, this is the highest humidity resistance so far reported for room temperature NO sensors.^[18] Interestingly, although HNG-ethanol performed the highest response under 25% relative humidity, it only recovered to 90% of the initial value (**Figure S5**, Supporting Information). The reason for this could be that the dissolving of NO in the adsorbed water on the surface of electrode would improve the sensing performance of HNG-ethanol,^[19] but simultaneously reduce the diffusion speed of NO in the recovery process.

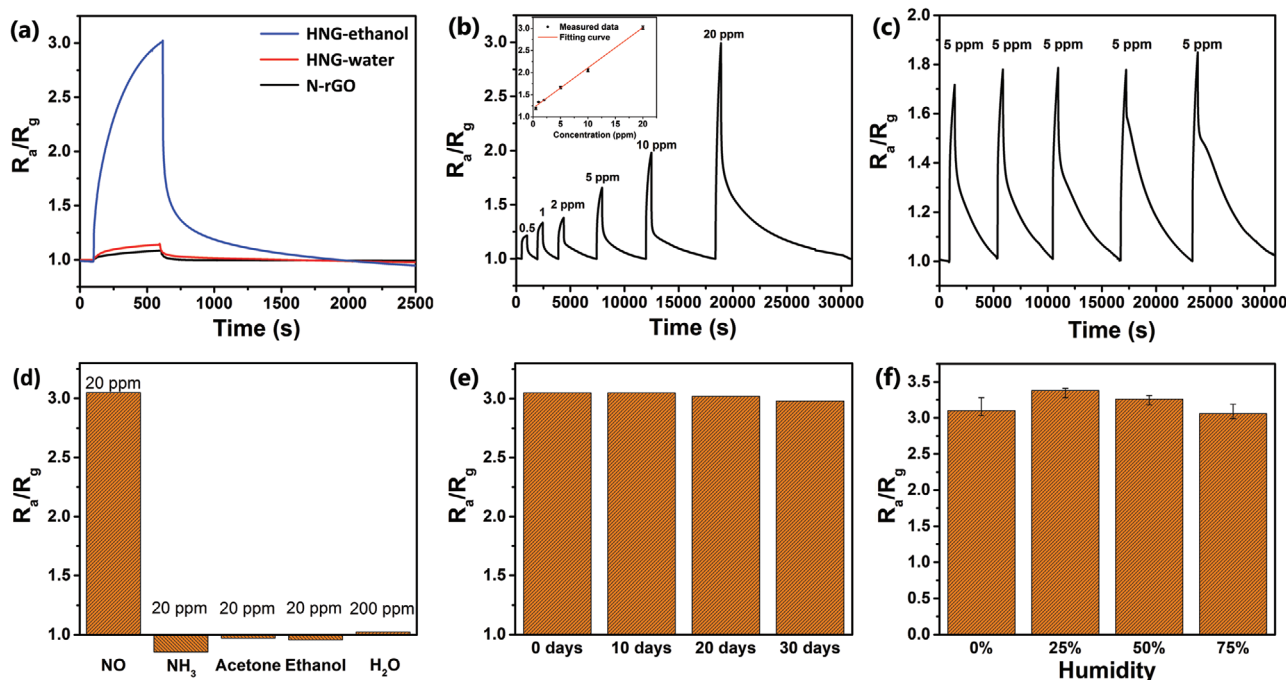


Figure 2. a) Response curves of N-rGO (black), HNG-ethanol (blue), and HNG-water (red) sensors toward 20 ppm of NO. b) Successive response curve of HNG-ethanol sensors to different NO concentrations ranging from 0.5 to 20 ppm. Inset: corresponding linear fit of the responses of NO concentration (R -square = 0.99782). Error bars for the data points lie within the symbols themselves. c) Cyclic response curve of HNG-ethanol sensors upon exposure to 5 ppm of NO and interferential gases, including NH₃, acetone, ethanol, and 200 ppm of H₂O. d) Selective response of the HNG-ethanol sensors toward 20 ppm of NO and interferential gases, including NH₃, acetone, ethanol, and 200 ppm of H₂O. e) Aging test of HNG-ethanol sensors toward 20 ppm of NO for 30 days. f) Response of HNG-ethanol toward 20 ppm of NO under 0–75% relative humidity. Error bars for the data points lie within the symbols themselves.

It is usually cognized that good dispersity of active sites on the planar configuration of conventional 2D materials would benefit the gas sensing performance of the materials.^[20] However, large crystalline aggregates of Hemin accidentally appeared on the graphene nanosheets of HNG-ethanol, and seemingly played the key role in this work. Which factor influence most on the sensing performance of

HNG-ethanol, the structure of Hemin aggregates, or the inner interaction between Hemin and graphene?

To investigate this question, XPS spectra of HNG-ethanol and HNG-water were obtained and shown in Figure 3. The survey spectra of both samples (Figure 3a,b) verified the presence of carbon, oxygen, nitrogen and iron. Firstly, the high-resolution spectra of C 1s of HNG-ethanol was shown in

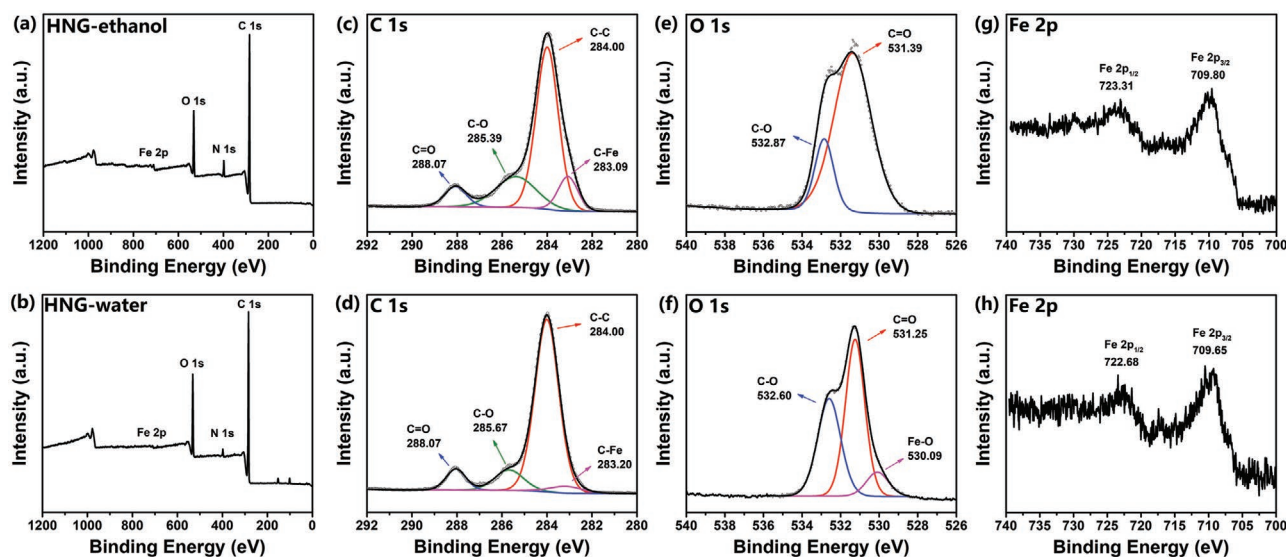


Figure 3. XPS spectra of HNG-ethanol and HNG-water: Survey spectra of a) HNG-ethanol and b) HNG-water; high resolution spectra of C 1s of c) HNG-ethanol and d) HNG-water; O 1s of e) HNG-ethanol and f) HNG-water; Fe 2p of g) HNG-ethanol and h) HNG-water.

Table 1. Performances of similar room temperature NO gas sensors based on metal derivatives (metal oxide, metal nanoparticles, metal complex, etc.).

Materials	NO concentration [ppm]	Response (R_a/R_g or R_g/R_a)	UV illumination	Response/recovery time [s]	LOD	Ref.
Coralline-like porous ZnO	40 ppm	23.59	/	331/1285	5 ppm	[8a]
CS-MoS ₂	1 ppm	2.65	$\lambda = 365$ nm	50/ \approx 1300	0.06 ppm	[8b]
TiO ₂ @NGQDs	100 ppm	1.31	$\lambda = 365$ nm	235/285	10 ppm	[8c]
3D-hierarchical WSe ₂ nanoscrews	1 ppm	\approx 2.0	/	120/ \approx 400	0.06 ppm	[8d]
CNFs/CoS ₂ /MoS ₂	10 ppm	\approx 1.045	/	1200/6000	1 ppm	[16]
MoS ₂	100 ppm	1.72	$\lambda = 254$ nm	\approx 200/ \approx 550	10 ppm	[17]
N-rGO-Hemin	1 ppm	1.34	/	400/1000	0.5 ppm	This work

Figure 3c. Four peaks centered at 288.07, 285.39, 284.00, and 283.09 eV were attributed to C=O, C–O, C–C, and C–Fe bonds respectively,^[21] which was quite surprising since few literature was concerned about the C–Fe bonds existing in conventional metal (nanoparticles/oxide/complex)-graphene based materials. In contrast, in the high-resolution spectra of the C 1s of HNG-water (Figure 3d), the intensity of the peak corresponded to C–Fe bond around 283.20 eV was very weak, indicating that much less Hemin were chemically combined with N-rGO in aqueous solution. Second, in Figure 3e, the high-resolution spectra of the O 1s of HNG-ethanol revealed the peaks at 532.87 and 531.39 eV, assigned to C–O and C=O bonds respectively. Besides, an extra peak at 530.09 eV was found in the O 1s spectra of HNG-water in Figure 3f, which was assigned to Fe–O bond. Third, the peaks of Fe 2p_{3/2} band (709.80 eV) and Fe 2p_{1/2} band (723.31 eV) were presented in the high-resolution spectra of Fe 2p of HNG-ethanol (Figure 3g). Herein, it is worth noting that the binding energy of Fe 2p_{3/2} band and Fe 2p_{1/2} band in HNG-water (Figure 3h) slightly differed from which in HNG-ethanol, illustrating the different interrelation of Fe with surrounding atoms.

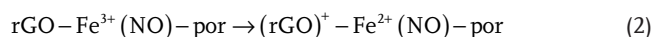
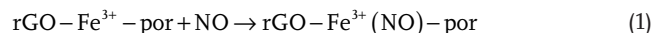
It could be concluded that the surprising distinction between the bonding status of Fe atoms in the two samples resulted in their significantly different sensing performances. Especially, it would be crucial to demonstrate whether or not the C–Fe bond plays the KEY role in the sensing process of HNG-ethanol sensor. As reported by Pagola, Hemin aggregates are built of hydrogen-bonded head-to-tail dimers, in which the central iron ion within the porphyrin ring of one Hemin coordinates with a carboxylate oxygen of a second Hemin.^[22] Later researches generally produced crystalline Hemin by adding a Hemin-NaOH solution into its poor solvents such as alcohols, triggered by the attachment of the first Hemin molecule to a smooth surface.^[15a,23] Different from above, referred to Egan's work, hydroxyl ions can combine with iron ions in aqueous solution, then the Fe–O–Fe bond will form in the Hemin dimers under high pH condition.^[24] Hence, it is reasonable that there be C–Fe bonding happening between Hemin and graphene on the surface of graphene nanosheets in non-aqueous solvent such as ethanol, while hindered by the hydroxyl ions in aqueous solution.

A possible mechanism of the formation of C–Fe bond was then proposed in **Scheme 2**. Carboxylic groups of graphene oxide are eliminated via decarboxylation during the solvothermal process (i), which produces carbonanions (ii).^[25] Subsequently, iron ions in porphyrin rings with positive charges

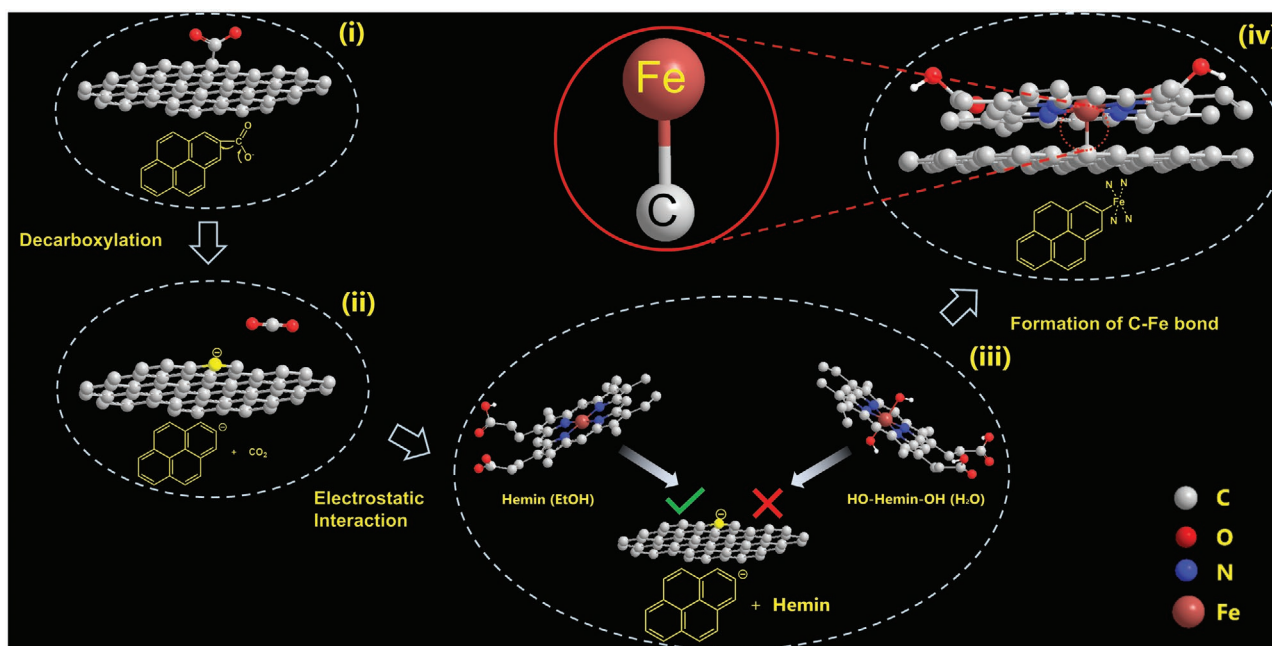
electrostatically interact with the carbonanions to form C–Fe bonds, while such process will hardly occur in aqueous solution due to the hindrance of hydroxyl ions (iii). At last, Hemin-N-rGO complexes are generated with C–Fe bonds as conjunctions (iv).

In addition, a hypothesis was proposed to interpret the appearance of the weak peak (283.20 eV) in the C 1s spectra of HNG-water (**Scheme 3**). The peak could be attributed to the small amount of C–Fe bonds with hydroxyl ions occupying the top sites of the Fe ions. These hydroxyl ions provide a steric hinderance, essentially impeding the contact of NO molecule with Hemin. This interpretation could also explain the decrease of the gas response in Figure 2f. The further increasing of humidity (>25%) would raise the amount of the hydroxyl ions from the adsorbed water around HNG-ethanol complexes, resulting in the formation of Fe–OH.

The formation process of C–Fe bond in HNG-ethanol was simulated by a density functional theory (DFT) calculation. A Hemin molecule and a polycyclic aromatic hydrocarbon with a carbanion sited at the edge were built in this model. After geometry optimization, the distance between Fe ion and the carbanion was 1.93 Å (**Figure 4a**), less than the sum (2.25 Å) of the covalent atomic radii of sp²-C (0.73 Å) and Fe³⁺ (1.52 Å) ion.^[26] Therefore, it could be concluded that a C–Fe chemical bond successfully formed in this model. In addition, **Figure 4b** displayed the electron localization function (ELF) map of HNG-ethanol, showing a high electron localization region existed between the carbanion and the Fe ion. Obviously, the majority of the electron cloud was distributed near the carbanion, which is similar with the electron distribution in adjacent N-Fe coordination bonds of Hemin, that is, the electron cloud is closed to the nitrogen atoms. Therefore, it could be proposed that coordination bond dominates the C–Fe bonding in this work.



As shown in **Figure 2d**, it is apparent that NO would act as an oxidizer in this sensing process based on the comparison with the typical reductive gas ammonia. Moreover,

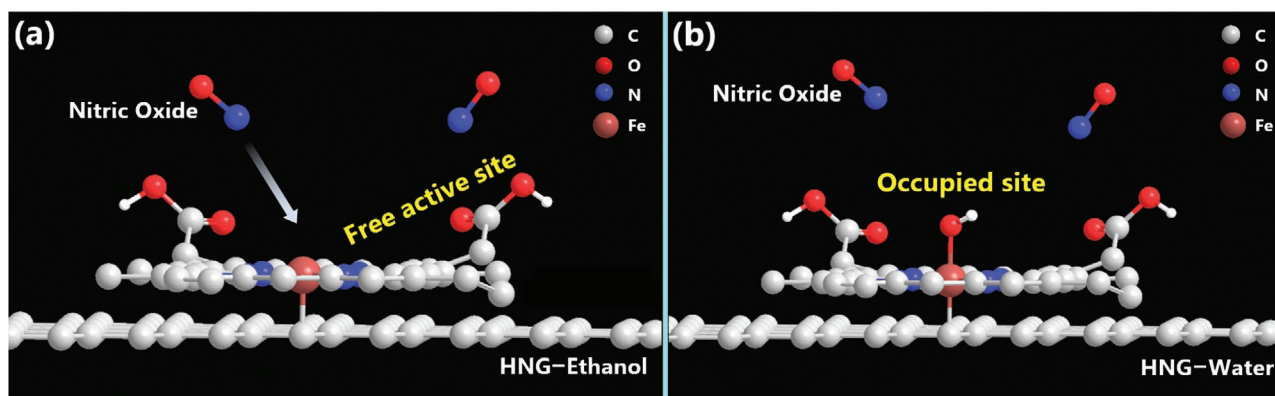


Scheme 2. Proposed mechanism of the formation of C–Fe bonds in HNG-ethanol.

the decreasing of the resistance of the as-prepared material once contacting with NO proves that HNG-ethanol behaviors as a p-type semiconductor. Thus, a possible mechanism of the catalyzed reduction of NO by iron was proposed as Equations (1)–(4). 1) NO is first absorbed onto the porphyrin ring of Hemin to contact with Fe^{3+} ion. 2) Benefiting from the strong electronegativity of NO, an electron is transferred from graphene to the Fe^{3+} ion of Hemin. 3) The electron is subsequently given to the NO molecule. The efficient transport of electrons through C–Fe bonds increases the amount of the holes on the p-type graphene nanosheets, which induces the decline of the resistance of the sensing material. More importantly, the C–Fe electron transport channel successfully empower Hemin with the capability to express the chemoresistive response toward NO gas. Whereas, much less C–Fe bonds exist in HNG-water with hydroxyl groups occupying the top sites of the Fe ions, leading to no response toward NO. 4) A complete recovery of the resistance of HNG-ethanol will

be realized by the removal of NO from the sensing system, accompany with the return of the electron to graphene.

To further understand the relationship between the sensing performance and the crystalline morphology of Hemin, control groups were carried out in EtOH/ H_2O mixed solutions with various volume ratios of 7:1, 6:2, and 4:4, respectively. The SEM images of all the above-mentioned samples including HNG-ethanol, HNG-7:1, HNG-6:2, HNG-4:4, and HNG-water were exhibited in **Figure 5**. Obvious crystalline Hemin were observed on all the graphene nanosheets of HNG-ethanol, HNG-7:1 and HNG-6:2, while only tiny pieces of crystals were found for HNG-4:4, and no crystal was observed for HNG-water. Two possible reasons for this phenomenon have been proposed. The hydroxyl ions in water bonded with Fe^{3+} ions will hinder the formation of the head-to-tail Hemin dimers for Hemin crystallization.^[22] On the other hand, higher proportion of water could improve the solubility of Hemin in the mixed solution, which is unbeneficial to the growth of the crystals.



Scheme 3. Illustration of the comparison between a) HNG-ethanol and b) HNG-water in the sensing process toward NO.

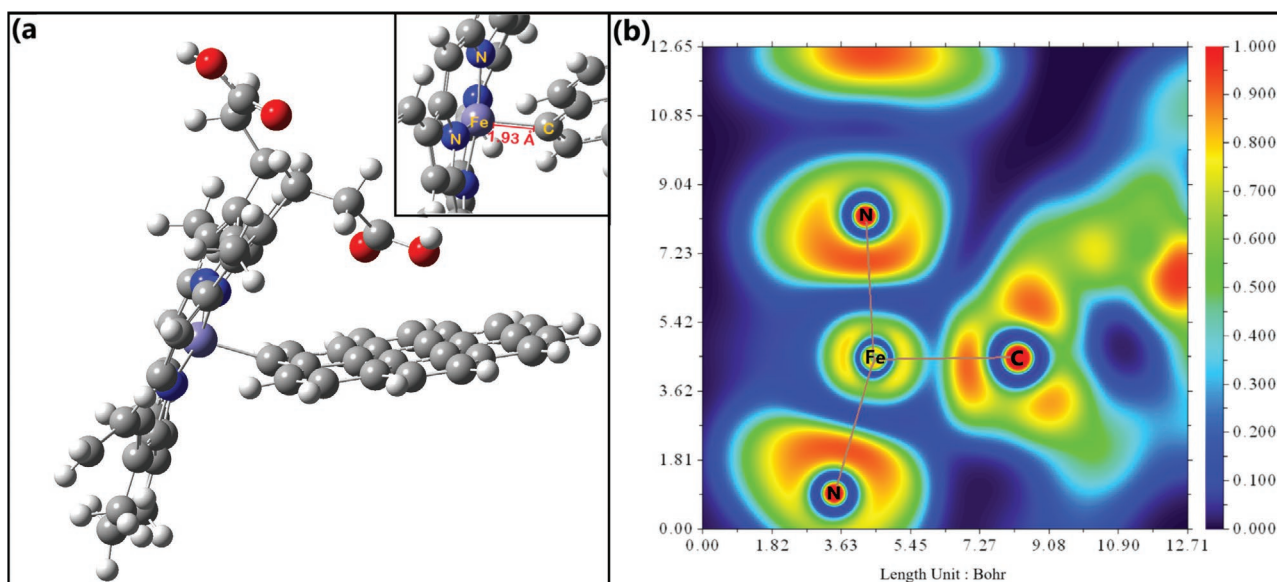


Figure 4. a) Geometry optimization of rGO and Hemin molecule showed the distance between C and Fe was 1.93 Å. b) Electron localization function (ELF) map of HNG-ethanol. The red color reveals the high electron localization nature in the bonding regions.

As revealed in Figure 5 and Figure S6, Supporting Information, the gas responses of the obtained five samples toward 20 ppm NO were not related with the proportion of water, neither with the morphology of crystalline Hemin. The high-resolution spectra of C 1s of all the five samples were also studied (Figure S7, Supporting Information) to confirm that the sensing performance of HNG-ethanol was positively correlated with the proportion of C–Fe bonds in the total carbon bonding. That is to say, more C–Fe electron transport channels will bring about higher gas response toward NO.

3. Conclusion

In summary, a complex (HNG-ethanol) of N-rGO and Hemin was successfully prepared via one-step solvothermal method. It was proposed that carbon–iron (C–Fe) bonds formed through the decarboxylation of graphene oxide and the electrostatic interaction between carbanion and Fe^{3+} . This unique C–Fe bonds play a crucial role in the gas sensing process by serving as electron transport channels between graphene and NO. Benefited from the existence of the C–Fe bonds, HNG-ethanol

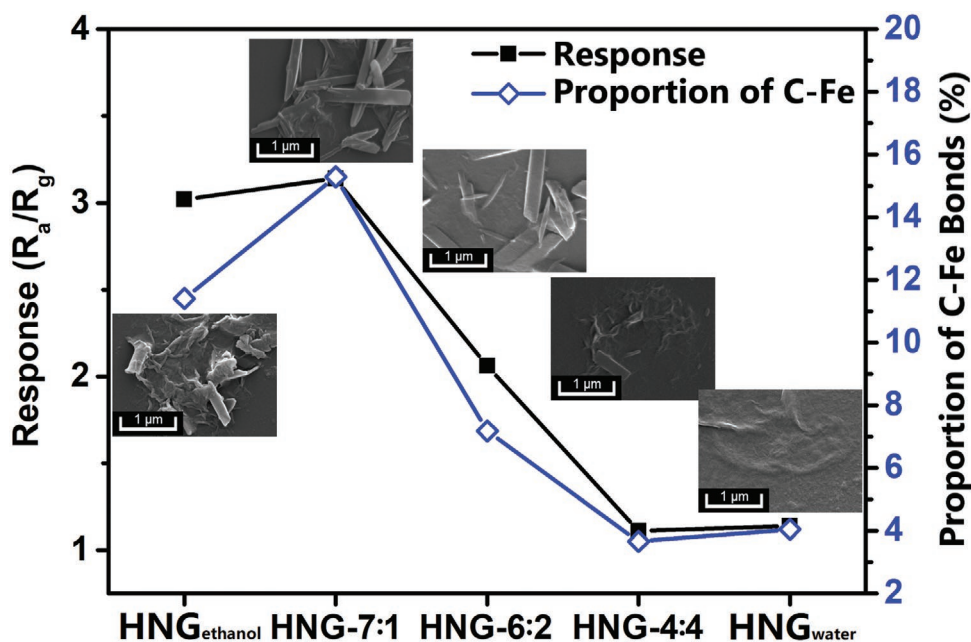


Figure 5. Response toward 20 ppm NO gas (black) and the proportion of C–Fe bonds in the C 1s spectra (blue) of HNG-ethanol, HNG-7:1, HNG-6:2, HNG-4:4, and HNG-water. The inner images were the corresponding SEM images of the series of HNG complex.

performed excellent gas sensing properties toward NO gas ($R_a/R_g = 3.05$, 20 ppm) with a practical LOD of 500 ppb and reliable repeatability (over 5 cycles). In addition, the HNG-ethanol sensor exhibited high selectivity against other exhaled gases, high humidity resistance, and stability (less than 3% decrease over 30 days). The strategy developed in this work would benefit the design and preparation of other metallic-carbon based functional materials such as sensing materials, single-atom catalysts, and energy storage materials.

4. Experimental Section

Materials: The high pure flake graphite (325 mesh) was purchased from XianFeng NANO Co., Ltd. Concentrated sulfuric acid (H_2SO_4 , 98%), hydrogen peroxide (H_2O_2 , 31%), Hemin, hydrogen peroxide ($NH_3 \cdot H_2O$, 25%), anhydrous ethanol, and potassium permanganate ($KMnO_4$) were purchased from Shanghai Titanchem Co., Ltd.

Preparation of Graphene Oxide (GO): GO was obtained from the high pure flake graphite by a modified Hummers' method. First, 23 mL of concentrated sulfuric acid were added to a beaker, and the solution was stirred in an ice bath until the temperature reached -1 to 1 °C. Subsequently, 1.0 g of high pure flake graphite was added into the solution, which was stirred for another 50 min. This step was followed by the slow addition of 6 g of $KMnO_4$ within 30 min, keeping the reaction temperature below 5 °C. The solution was further stirred for 3 h at a low temperature reaction stage. Afterward, the mixture was kept stirring in water bath at 40 °C for 45 min (moderate-temperature reaction stage). Next, the beaker was transferred into a water bath at 80 °C. 80 mL of deionized water was added into the solution successively, followed by further stirring in the water bath for 15 min. Then 60 mL of water was added to the solution for dilution. Afterward, the solution containing 60 mL of deionized water and 10.81 mL of H_2O_2 was added to end the reaction. It was then repeatedly centrifuged and washed with amount of water until the pH of the suspension was about 6. The final sediment was dispersed in 100 mL of deionized water and a brown homogeneous supernatant was collected.

Synthesis of Hemin-N-Doped Reduced Graphene Oxide (HNG-Ethanol): The HNG-ethanol hybrid composite was synthesized via a two-step solvothermal process. Typically, 5 mg of GO was dispersed in 8 mL of anhydrous ethanol, followed by ultrasonication for 10 min to form a brown solution. Next 30 mg of Hemin was added into the as-prepared suspension and another ultrasonication of 5 min was carried out. The optimized amount of Hemin was found by control experiments as shown in Figure S8 and Table S1, Supporting Information. Then, the mixture was subjected to vigorous stirring for 5 min and 240 μ L of ammonium hydroxide was added drop by drop. After refluxing at 80 °C for 10 h, the solution from the previous step was transferred to a 25 mL autoclave for further solvothermal reaction at 120 °C for 3 h. The resultant dispersion was rinsed twice by vacuum filtration with anhydrous ethanol. Finally, the solution was re-dispersed in 10 mL of anhydrous ethanol under mild ultrasonication. For comparison of gas-sensing performance, N-rGO was prepared through the same procedure mentioned above without adding Hemin. The preparation of the HNG-water was also similar with the preparation of the HNG-ethanol, the only difference was that the anhydrous ethanol was replaced by deionized water. Besides, the control groups with no nitrogen doping and employing DMF as solvent were carried out respectively, as shown in Figures S9 and S10, Supporting Information.

Characterization: The morphology of all the materials were observed using a scan electron microscope (SEM, Quanta 250 FEG, FEI, American) and a transmission electron microscope operated at 200 kV (JEM-2010, JEOL, Japan). Crystal structure was determined by X-ray powder diffraction (XRD; D8 Advance, Bruker, Germany), using Cu-K α as the incident radiation. Surface chemical groups were characterized by Fourier transform infrared (FT-IR) spectrophotometer (Vertex 70, Bruker, Germany) in a spectral range of 4000–400 cm^{-1} with the resolution of 2 cm^{-1} using potassium bromide (KBr) plate method. Raman spectra

were obtained by Raman microscope (inVia, RENISHAW, UK) under an excitation wavelength of 532 nm. Element composition was analyzed by X-ray photoelectron spectroscopy (XPS; Escalab 250Xi, Thermo Fisher, UK) with a mono X-Ray source Al K α as the incident radiation. Binding energy calibration was based on C 1s at 284.0 eV. The iron species' contents of hybrids were determined by the inductively coupled plasma atomic emission spectrometer (ICP-AES; SPECTRO ARCOS MV, SPECTRO, Germany).

Sensor Fabrication: The Ag–Pd interdigitated electrodes (IDEs) deposited on a ceramic substrate through screen printing technique were used to measure the gas-sensing properties. First, IDEs were cleaned with ethanol by ultrasonication for 30 min before using. 10 μ L of N-rGO, HNG-ethanol, and HNG-water were dropped onto the IDEs followed by drying in an oven at 75 °C for 15 min.

Gas-Sensing Measurement: The gas sensing measurements were performed using a Keithley 2450 Sourcemeter. A typical sensing test cycle consisted of three sequential steps. First, the IDEs were put into a blank chamber filled with dry air (R.H. \approx 20%) to record a baseline. Then, the IDEs were transferred into the sensing test chamber filled with target gas diluted in N_2 . Finally, the sensor was recovered in the blank chamber of dry air. All the measurements were carried out in ambient temperature (25 ± 2 °C).

DFT Calculation: In the theoretical calculation, geometry optimizations were performed using the B3LYP exchange-correlation functional with Grimme's DFT-D3(BJ) empirical dispersion correction.^[27] The def2-TZVP basis set was performed for Fe element, and 6–311G* basis set was adopted for other elements. The DFT calculations were performed with Gaussian and analyzed by Multiwfn.^[28]

Supporting Information

Supporting Information is available from the Wiley Online Library or from the author.

Acknowledgements

Y.G. and J.W. contributed equally to this work. This work was supported by National Natural Science Foundation of China (Grant No. 51973070), Guangdong Basic and Applied Basic Research Foundation (No. 2021A1515012420), Science and Technology Program of Guangzhou (No. 2019050001), Innovative Team Project of Education Bureau of Guangdong Province, Startup Foundation from SCNU, Guangdong Provincial Key Laboratory of Optical Information Materials and Technology (No. 2017B030301007), the 111 Project.

Conflict of Interest

The authors declare no conflict of interest.

Data Availability Statement

The data that support the findings of this study are available from the corresponding author upon reasonable request.

Keywords

carbon–iron bonds, gas sensors, graphene, Hemin, nitric oxide

Received: June 4, 2021
Revised: December 5, 2021
Published online: January 20, 2022

- [1] a) T. J. McMahon, R. E. Moon, B. P. Luschinger, M. S. Carraway, A. E. Stone, B. W. Stolp, A. J. Gow, J. R. Pawloski, P. Watke, D. J. Singel, C. A. Piantadosi, J. S. Stamler, *Nat. Med.* **2002**, *8*, 711; b) E. Terasaka, K. Yamada, P. H. Wang, K. Hosokawa, R. Yamagiwa, K. Matsumoto, S. Ishii, T. Mori, K. Yagi, H. Sawai, H. Arai, H. Sugimoto, Y. Sugita, Y. Shiro, T. Tosha, *Proc. Natl. Acad. Sci. USA* **2017**, *114*, 9888.
- [2] a) L. E. Gustafsson, A. M. Leone, M. G. Persson, N. P. Wiklund, S. Moncada, *Biochem. Biophys. Res. Commun.* **1991**, *181*, 852; b) K. Alving, E. Weitzberg, J. M. Lundberg, *Eur. Respir. J.* **1993**, *6*, 1368; c) R. A. Dweik, P. B. Boggs, S. C. Erzurum, C. G. Irvin, M. W. Leigh, J. O. Lundberg, A.-C. Olin, A. L. Plummer, D. R. Taylor, *Am. J. Respir. Crit. Care Med.* **2011**, *184*, 602; d) Global Initiative for Asthma **2019**. <https://ginasthma.org/wpcontent/uploads/2019/06/GINA-2019-main-report-June-2019-wms.pdf> (accessed: June 2019).
- [3] a) A. L. Kleschyov, P. Wenzel, T. Munzel, *J. Chromatogr. B* **2007**, *851*, 12; b) K. Liu, J. Mei, W. Zhang, W. Chen, X. Gao, *Sens. Actuators, B* **2017**, *251*, 632; c) Y. Wang, M. Nikodem, E. Zhang, F. Cikach, J. Barnes, S. Comhair, R. A. Dweik, C. Kao, G. Wysocki, *Sci. Rep.* **2015**, *5*, 9096.
- [4] a) Y. Yong, X. Su, Q. Zhou, Y. Kuang, X. Li, *Sci. Rep.* **2017**, *7*, 17505; b) B. Zhang, J.-Y. Sun, P.-X. Gao, *ACS Sens.* **2021**, *6*, 2979; c) M.-Y. Kim, M. H. Naveen, N. G. Gurudatt, Y.-B. Shim, *Small* **2017**, *13*, 1700502.
- [5] a) Y. Hu, X. Hu, J. Qiu, W. Quan, W. Qin, X. Min, S. Lu, S. Chen, W. Du, X. Chen, W. Zhang, *ACS Appl. Mater. Interfaces* **2018**, *10*, 42583; b) N. Tammanoon, T. Iwamoto, T. Ueda, T. Hyodo, A. Wisitsoraat, C. Liewhiran, Y. Shimizu, *ACS Appl. Mater. Interfaces* **2020**, *12*, 41728.
- [6] a) Y. Liu, Y. Jiao, Z. Zhang, F. Qu, A. Umar, X. Wu, *ACS Appl. Mater. Interfaces* **2014**, *6*, 2174; b) Z. Ma, K. Yang, C. Xiao, L. Jia, *J. Hazard. Mater.* **2021**, *416*, 126118.
- [7] a) W.-L. Jiang, Y. Li, H.-W. Liu, D.-Y. Zhou, O.-Y. Juan, L. Yi, C.-Y. Li, *Talanta* **2019**, *197*, 436; b) J. Miao, Y. Huo, X. Lv, Z. Li, H. Cao, H. Shi, Y. Shi, W. Guo, *Biomaterials* **2016**, *78*, 11.
- [8] a) N. Huang, Y. Cheng, H. Li, L. Zhao, Z. He, C. Zhao, F. Liu, L. Ding, *J. Colloid Interface Sci.* **2019**, *556*, 640; b) Y. Z. Chen, S. W. Wang, C. C. Yang, C. H. Chung, Y. C. Wang, S. W. Huang, C. W. Chen, T. Y. Su, H. N. Lin, H. C. Kuo, Y. L. Chueh, *Nanoscale* **2019**, *11*, 10410; c) G. Murali, M. Reddeppa, C. Seshendra Reddy, S. Park, T. Chandrakalavathi, M. D. Kim, I. In, *ACS Appl. Mater. Interfaces* **2020**, *12*, 13428; d) Y.-Z. Chen, S.-H. Lee, T.-Y. Su, S.-C. Wu, P.-J. Chen, Y.-L. Chueh, *J. Mater. Chem. A* **2019**, *7*, 22314.
- [9] a) M. D. Brown, M. H. Schoenfish, *Electrochim. Acta* **2018**, *273*, 98; b) Y.-L. Liu, X.-Y. Wang, J.-Q. Xu, C. Xiao, Y.-H. Liu, X.-W. Zhang, J.-T. Liu, W.-H. Huang, *Chem. Sci.* **2015**, *6*, 1853; c) X. Liu, D. Huang, C. Lai, L. Qin, G. Zeng, P. Xu, B. Li, H. Yi, M. Zhang, *Small* **2019**, *15*, 1900133.
- [10] T. Q. Nguyen, M. C. S. Escano, H. Kasai, *J. Phys. Chem. B* **2010**, *114*, 10017.
- [11] a) T. Nyokong, S. Vilakazi, *Talanta* **2003**, *61*, 27; b) S. Yang, M. E. Meyerhoff, *Electroanalysis* **2013**, *25*, 2579; c) A. Sarkar, E. L. Carter, J. B. Harland, A. L. Speelman, N. Lehnert, S. W. Ragsdale, *Proc. Natl. Acad. Sci. U. S. A.* **2021**, *118*, e2016717118.
- [12] a) F. Schedin, A. K. Geim, S. V. Morozov, E. W. Hill, P. Blake, M. I. Katsnelson, K. S. Novoselov, *Nat. Mater.* **2007**, *6*, 652; b) N. Yue, J. Weicheng, W. Rongguo, D. Guomin, H. Yifan, *J. Mater. Chem. A* **2016**, *4*, 8198; c) Z. Chen, J. Wang, A. Umar, Y. Wang, H. Li, G. Zhou, *ACS Appl. Mater. Interfaces* **2017**, *9*, 11819; d) Z. Chen, J. Wang, D. Pan, Y. Wang, R. Noetzel, H. Li, P. Xie, W. Pei, A. Umar, L. Jiang, N. Li, N. F. Rooij, G. Zhou, *ACS Nano* **2018**, *12*, 2521.
- [13] a) Z. Sun, Z. Yan, J. Yao, E. Beitler, Y. Zhu, J. M. Tour, *Nature* **2010**, *468*, 549; b) J. Qiu, X. Hu, X. Min, W. Quan, R. Tian, P. Ji, H. Zheng, W. Qin, H. Wang, T. Pan, S. Cheng, X. Chen, W. Zhang, X. Wang, *ACS Appl. Mater. Interfaces* **2020**, *12*, 19755.
- [14] a) X. Liu, C. Z. Wang, Y. X. Yao, W. C. Lu, M. Hupalo, M. C. Tringides, K. M. Ho, *Phys. Rev. B* **2011**, *83*, 235411; b) D. Cortes-Arriagada, L. Sanhueza, A. Bautista-Hernandez, M. Salazar-Villanueva, E. C. Anota, *J. Phys. Chem. C* **2019**, *123*, 24209; c) Y. Tang, W. Chen, Z. Wang, G. Zhao, Y. Cui, Z. Li, Y. Li, Z. Feng, X. Dai, *Appl. Surf. Sci.* **2020**, *530*, 147178; d) Y. Li, Z. Zhou, G. Yu, W. Chen, Z. Chen, *J. Phys. Chem. C* **2010**, *114*, 6250.
- [15] a) K. N. Olafson, J. D. Rimer, P. G. Vekilov, *Cryst. Growth Des.* **2014**, *14*, 2123; b) I. Weissbuch, L. Leiserowitz, *Chem. Rev.* **2008**, *108*, 4899.
- [16] S. Hou, R. Pang, S. Chang, L. Ye, J. Xu, X. Wang, Y. Zhang, Y. Shang, A. Cao, *ACS Appl. Mater. Interfaces* **2020**, *12*, 29778.
- [17] S. Ramu, T. Chandrakalavathi, G. Murali, K. S. Kumar, A. Sudharani, M. Ramanadha, K. R. Peta, R. Jeyalakshmi, R. P. Vijayalakshmi, *Mater. Res. Express* **2019**, *6*, 085075.
- [18] a) Z. Meng, A. Aykanat, K. A. Mirica, *J. Am. Chem. Soc.* **2019**, *141*, 2046; b) G. Madhaiyan, T.-W. Tung, H.-W. Zan, H.-F. Meng, C.-J. Lu, A. Ansari, W.-T. Chuang, H.-C. Lin, *Sens. Actuators B* **2020**, *320*, 128392;
- [19] K. Asanuma, S. Hino, Y. Y. Maruo, *Microchem. J.* **2019**, *151*, 104251.
- [20] a) Z. Chen, A. Umar, S. Wang, Y. Wang, T. Tian, Y. Shang, Y. Fan, Q. Qi, D. Xu, L. Jiang, *Nanoscale* **2015**, *7*, 10259; b) M. M. Mohammadi, A. Kumar, J. Liu, Y. Liu, T. Thundat, M. T. Swihart, *ACS Sens.* **2020**, *5*, 2344; c) R. Tian, S. Wang, X. Hu, J.-G. Zheng, P. Ji, J. Lin, J. Zhang, M. Xu, J. Bao, S. Zuo, H. Zhang, W. Zhang, J. Wang, L. Yu, *J. Mater. Chem. A* **2020**, *8*, 23784.
- [21] J. Li, H. Lan, H. Liu, G. Zhang, X. An, R. Liu, J. Qu, *ACS Appl. Mater. Interfaces* **2019**, *11*, 15709.
- [22] S. Pagola, P. W. Stephens, D. S. Bohle, A. D. Kosar, S. K. Madsen, *Nature* **2000**, *404*, 307.
- [23] K. N. Olafson, M. A. Ketchum, J. D. Rimer, P. G. Vekilov, *Cryst. Growth Des.* **2015**, *15*, 5535.
- [24] C. Asher, K. A. de Villiers, T. J. Egan, *Inorg. Chem.* **2009**, *48*, 7994.
- [25] X. Gao, J. Jang, S. Nagase, *J. Phys. Chem. C* **2010**, *114*, 832.
- [26] B. Cordero, V. Gomez, A. E. Platero-Prats, M. Reves, J. Echeverria, E. Cremades, F. Barragan, S. Alvarez, *Dalton Trans.* **2008**, *21*, 2832.
- [27] L. Goerigk, S. Grimme, *J. Chem. Theory Comput.* **2011**, *7*, 291.
- [28] T. Lu, F. Chen, *J. Comput. Chem.* **2012**, *33*, 580.